Journal of Advances in Medicine and Medical Research

22(5): 1-24, 2017; Article no.JAMMR.30457
Previously known as British Journal of Medicine and Medical Research
ISSN: 2231-0614, NLM ID: 101570965

The Effect of Fluid-structure Interaction in Finite-element Analysis of Skull Bone on Relieving Cerebral Injury in a Porcine Model

Xian Fang Yue[1,2], Duncan E. T. Shepherd[1*], Daniel M. Espino[1], Li Wang[2] and Hongwu Meng[2]

[1]School of Mechanical Engineering, University of Birmingham, Edgbaston, Birmingham B15 2TT, UK.
[2]School of Mechanical Engineering, University of Science and Technology Beijing, Beijing 100083, China.

Authors' contributions

This work was carried out in collaboration between all authors. All authors read and approved the final manuscript.

Article Information

DOI: 10.9734/JAMMR/2017/30457
Editor(s):
(1) Rodrigo Crespo Mosca, Department of Biotechnology, Institute of Energetic and Nuclear Research (IPEN-CNEN), University of Sao Paulo (USP), Brazil.
Reviewers:
(1) Y. Kiran Kumar, Philips Electronics India Ltd, Bangalore, India.
(2) Danladi Sambo Amaza, Kaduna State University, Kaduna, Nigeria.
(3) Syed A. Jamal, University of Missouri, Kansas City, USA.
(4) M. Alvaro Valencia, Universidad de Chile, Chile.
(5) Toshihiro Sera, Kyushu University, Japan.
Complete Peer review History: http://www.sciencedomain.org/review-history/19675

Original Research Article

Received 10th November 2016
Accepted 29th May 2017
Published 23rd June 2017

ABSTRACT

Introduction: Bone tissue is non-homogeneous, porous and anisotropic. Compact bone contains a hierarchical structure of interconnected channels, and cancellous bone is the spongy construction with the biphasic of viscous fluid and elastic solid materials. Fluid flow in and out has also been suggested to play a role in the mechanosensory system of bone.
Objective: To investigate the influence of interstitial fluid on the microstructural skeleton of compact and cancellous skull bone by finite-element simulation with the changing intracranial pressure.
Methods: Scanning Electron Microscopy (SEM) was adopted to determine the microstructural

**Corresponding author: E-mail: d.e.shepherd@bham.ac.uk;*
E-mail: yuexf@me.ustb.edu.cn;

parameters of fresh porcine skull bone, which used to create a microscopic model of skull bone subjected to a fluid-solid interaction analysis.
Results: Simulations were performed with and without Fluid-Structure Interaction (FSI). The strain and stress rate of the skull-bone microstructure increased with the tissue fluid by 38.5% and 21.5%, respectively. Especially for compact skull bones, the microstructure strain and stress rate were greater by 1.42 to 2.49 times and 1.39 to 2.42 times, respectively, when the tissue fluid flow was included.
Conclusion: In conclusion, the deformation of skull bone tissue is enhanced with the increase of interstitial fluid under the same pressure, which would absorb more impact on cerebral injury caused by intracranial hypertension. Conversely, the load-bearing of bone tissue is enhanced with the increase of solid bone skeleton under the same pressure. During the analysis on mechanical properties of skull bone with FSI, the compact and cancellous bones are not regarded as a single phase solid structure and the porous material characteristics must be considered.

Keywords: Biomechanics; bone remodelling; finite - element analysis; fluid-structure interaction; human skull.

1. INTRODUCTION

Intracranial hypertension is a common neurologic complication in critically ill patients [1], including patients with severe TBI [2]; it is associated with poor prognosis and with high rates of mortality [3]. Intracranial hypertension has been reported to occur in 25–40% of patients with severe TBI [4]. Data on causes of death from the 1990s have shown that cerebrovascular diseases remain a leading cause of death. In 2001 it was estimated that cerebrovascular diseases (stroke) accounted for 5.5 million deaths worldwide, equivalent to 9.6% of all deaths [5]. Many surviving stroke patients will often depend on other people's continuous support to survive. Increased intracranial pressure (ICP) can arise for a variety of reasons such as trauma to the head and brain tumours [6,7]. Previous studies have been carried out on the relationship between ICP and deformation of cranial cavity [8]. The objective of this study was to investigate the relationships between the microstructural skeleton, tissue fluid and deformation properties of compact and cancellous skull bone in the primary anatomic directions in such a way as to minimize hydraulic interactions described by finite element method. There exist a lot of models simulating the whole head system and its dynamical characteristics, each one of which makes some simplifications as far as geometric and/or physical properties are concerned. However, almost all these approaches try to identify how a specific factor, characterizing the head system, is involved into the injury and recovery procedure, oversimplifying simultaneously the other factors. This approach has the disadvantage that it cannot deal with the interference of the several parameters participating in the dynamical behaviour of the human head [9-11]. Every component simulated by fluid was characterized by harmonic motion represented suitably through potential functions. Considering the functions characterizing the motion of several materials as solutions of the corresponding partial differential equations and imposing on these solutions the suitable boundary conditions on discontinuity surfaces of head-brain system [12-17], we had to face the problem of head dynamic characteristics as a complicated boundary value problem. At first, a mathematical analysis is carried out for the study of the dynamic characteristics of the human skull-brain system in the framework of the three-dimensional theory of elasticity, and further study is needed to simulate the real physical system. However, because of a lack of quantitative data on brain-skull material properties, boundary conditions and deformations, the predictions of mathematical models remain uncertain [18,19]. The complexity of the human skull structure presents an extremely difficult task to one wishing to perform detailed simulation of the physical processes of the human head by mathematical modelling [20-23]. Although the finite-element model representations of the head geometry are more desirable, compatible characterizations of the zonal scalp, skull, dura mater, and brain constitutive properties along with engineering definitions of the associated interface conditions are lacking [24-26].

As a strong layer, bones are helping to keep some organs in the human body safe when people get hurt [27]. Identically, the function of human skull is mainly protecting the brain – the most important organ in the human body which

needs lots of protection [28-32]. Generally, each cranial bone contains two forms of tissue: External compact bone and inside cancellous bone [33]. Compact bone is thickest and relatively compact, and the cancellous bone is the spongy construction with the biphasic of viscous fluid and elastic solid materials [34,35]. Fluid flow in and out has also been suggested to play a role in the mechanosensory system of bone [36-40].

Skull fractures are the break in the cranial bone, also known as the skull, and injury, tumour invasion, or infection can cause the cranial defects. An injury to the brain can also accompany the fracture. Increased intracranial pressure (ICP) can arise for a variety of reasons such as trauma to the head and brain tumours. Mathematical models of cranial cavity biomechanics are being developed to simulate the mechanics of cranial injury and to design monitoring devices. Mathematical modelling and computer simulations can illuminate the mechanics of cranial injury, but only if the parameters of the model are accurate. The main material properties include elastic modulusb, ultimate stress, and ultimate strain, which dictate the response and failure of skull bone and brain to loading. It will not only provide insight into the reaction of cranial cavity to ICP-induced loading, but also improve the accuracy of skull fracture impacts to a head determining the material properties of skull bone. Increased intracranial pressure (ICP) can arise for a variety of reasons such as trauma to the head and brain tumours [41,42]. Prolonged intracranial hypertension, a common pathway in the presentation of traumatic head injury, can lead to brain damage or even death [43,44]. Previous studies have been carried out on the relationship between ICP and deformation of cranial cavity [45]. Compact bone has many canals for nerves and blood vessels [34]. Cancellous bone has open sections called pores, which are filled with marrow, nerves and blood vessels that carry cells and nutrients in and out of the bone [35]. This paper presents a computational model of the skull that considers Fluid-Structure Interaction (FSI) from the micro-structure.

2. MATERIALS AND METHODS

The analysis and simulation for the study are shown in Fig. 1. SEM with the Image-Pro software was adopted to determine the microstructural parameters about fresh specimens of porcine skull bone [46]. Then the finite-element (FE) software ANSYS and Fluent was used to create a microscopic model of skull bone subjected to a fluid-solid interaction analysis [47]. Under the condition of the ICP-induced interstitial fluid flow, the deformations of compact and cancellous skull bone were analysed and the effect of FSI in the porcine skull bone on relieving cerebral injury. Finally, the microstructural parameters could be verified based on the FE analysis of compact and cancellous skull bone.

2.1 SEM Testing

2.1.1 Preparation of porcine skull specimens

Fresh porcine skulls were used to study how the porous structure of skull bone affects its deformation. Specimens of compact and cancellous bone were obtained and subjected to cleaning, fixing, degreasing, dehydration and drying [41]. The reagents used were Anhydrous ethanol (≥99.9%), Formaldehyde (40%), Physiological saline (0.9%), and Sodium hypochlorite (≥99.9%) (National Pharmaceutical Group Chemical Reagent Co. Ltd).

After rinsing with physiological saline, the specimens were fixed for 24 h in 10% Formaldehyde solution. The specimens were then removed and washed with Formaldehyde for 10 minutes at room temperature, and were treated for 30 minutes with 10% sodium hypochlorite solution containing 10% active chlorine [48,49]. The specimens were dehydrated using anhydrous ethanol at different concentrations of 30%, 50%, 70%, 80%, and 100%. Each alcohol concentration was used for 3 h to 5 h after which the specimens were dried for 40 min using critical-point drying apparatus (HWS-150, Suzhou Baojuntong Testing Equipment Co. Ltd).

2.1.2 Electron microscope scanning experiments of porcine skulls

The SEM images of the porous structures were shown in Fig. 2. Six specimens of porcine skull bones were used to obtain 3 compact bone specimens and 3 cancellous bone specimens.

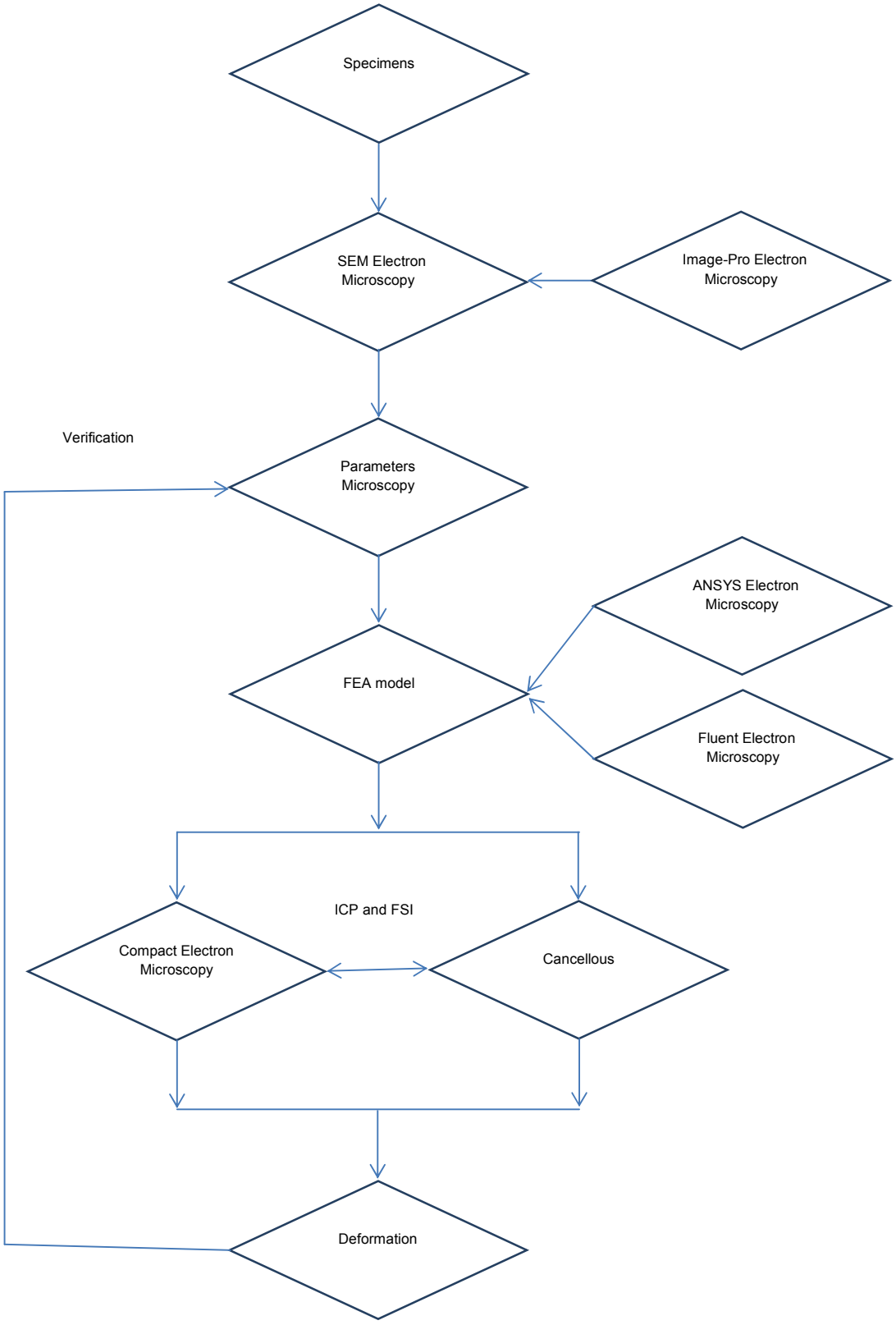

Fig. 1. Simulation flow-process diagram

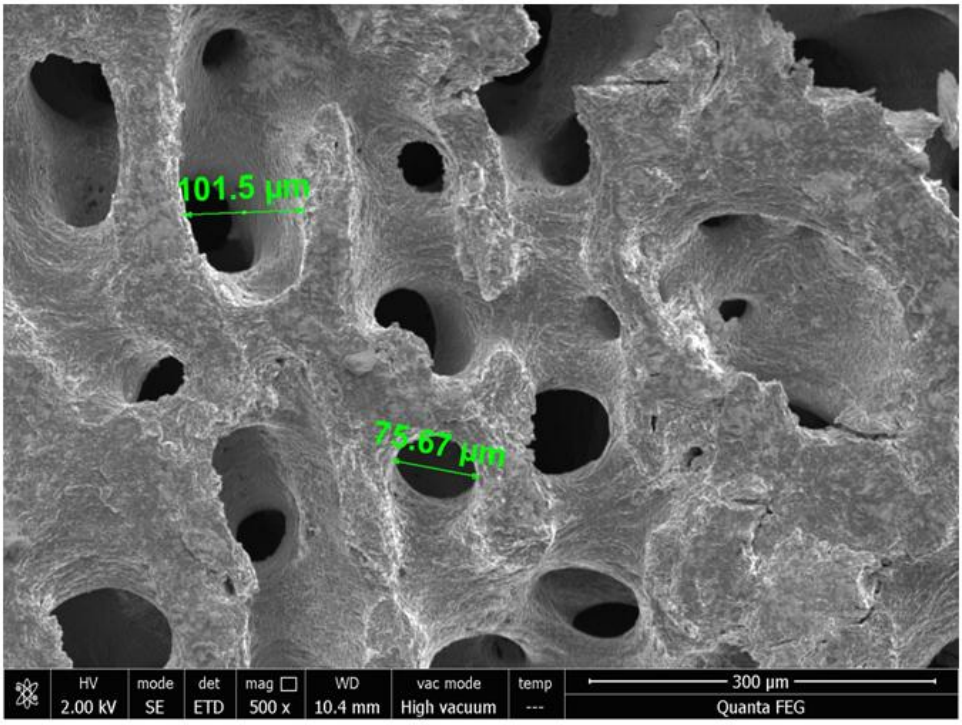

a) Scanning electron micrograph of the surface of porcine compact bone (500×)

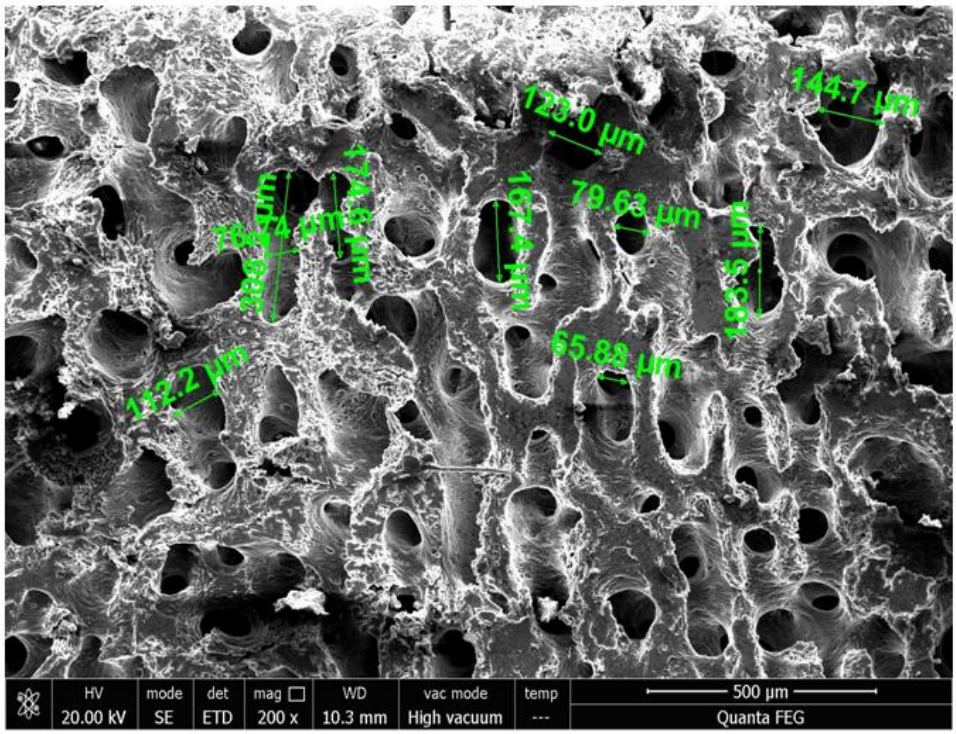

b) Scanning electron micrograph of the surface of porcine compact bone (200×)

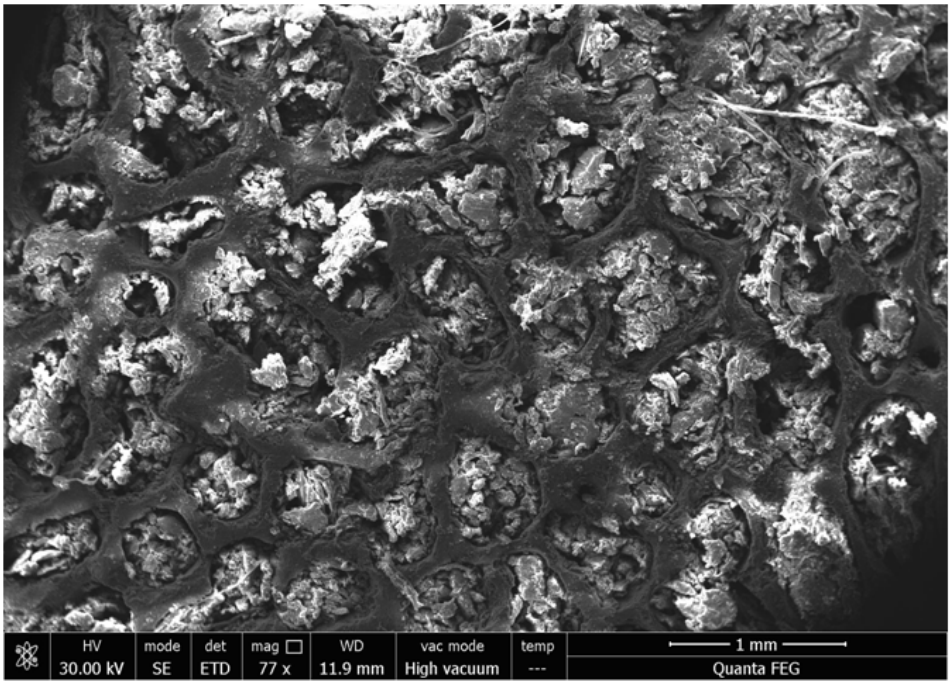

c) Scanning electron micrograph of the surface of porcine cancellous bone (77×)

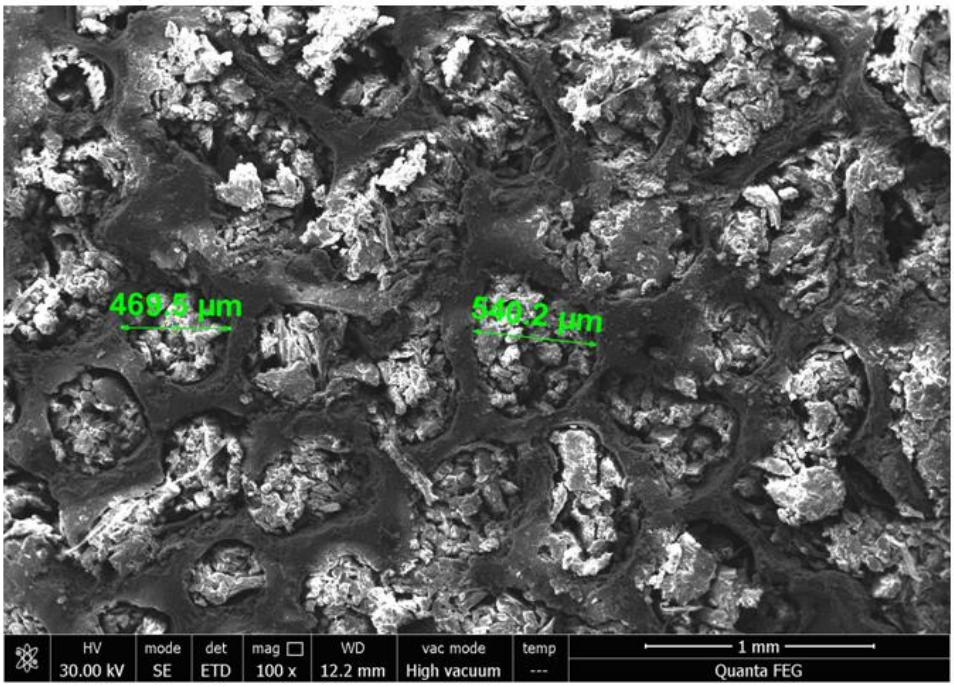

d) Scanning electron micrograph of the surface of porcine cancellous bone (100×)

Fig. 2. SEM photos of porcine compact and cancellous skull bone samples

a) SEM photo of compact bone with 500 magnification times, b) SEM photo of compact bone with 200 magnification times, c) SEM photo of cancellous bone with 77 magnification times, d) SEM photo of cancellous bone with 100 magnification times

2.1.3 Image-pro plus processing

To accurately obtain the parameters from the bone such as size, porosity, etc., the original electron microscope photos were pre-processed and then analysed. Scanning Electron Microscopy was used to image the specimens using an electron microscope with a desktop imaging system (Electron Scanning Microscope, S-3400N, Hitachi High Technologies America, Inc.; Energy Dispersive Spectroscopy, INCA Energy 350, Oxford Instruments, UK). Before imaging, specimens were sprayed with carbon for 10 to 15 minutes. The SEM images were then analysed using Image-Pro Plus processing software (Media Cybernetics, Silver Spring, Maryland 20910, USA).

For the SEM images of each skull specimen, the parameters of area, density, minimum and maximum radius and radius ratio were measured using the Image-Pro Plus processing software. Fig. 3 shows examples of the images. In the Image-Pro Plus processing software, the measurement area is defined by the colour range with the Select Colour function, and the colour background of the pictures was adjusted to achieve a smooth and uniform brightness.

Image-Pro Plus software was used to automatically count dark objects, measure area and mean diameter within an area of interest (AOI). Only objects within the AOI were counted from the resulting image. AOI's are a convenient way to isolate sampling regions or individual objects when counting. The objects touching the boundary are only partially counted. For the porcine skull bone, a grey-scale threshold was set to separate the solid skeleton from the pores in the SEM images. Thus, the structure and porosity of the microstructure of the skull bone can be calculated.

The porosities of compact bone from skull specimens are shown in Table 1. The pore parameters of porcine compact and cancellous skull bones were calculated at the different magnifications (Tables 1 - 3).

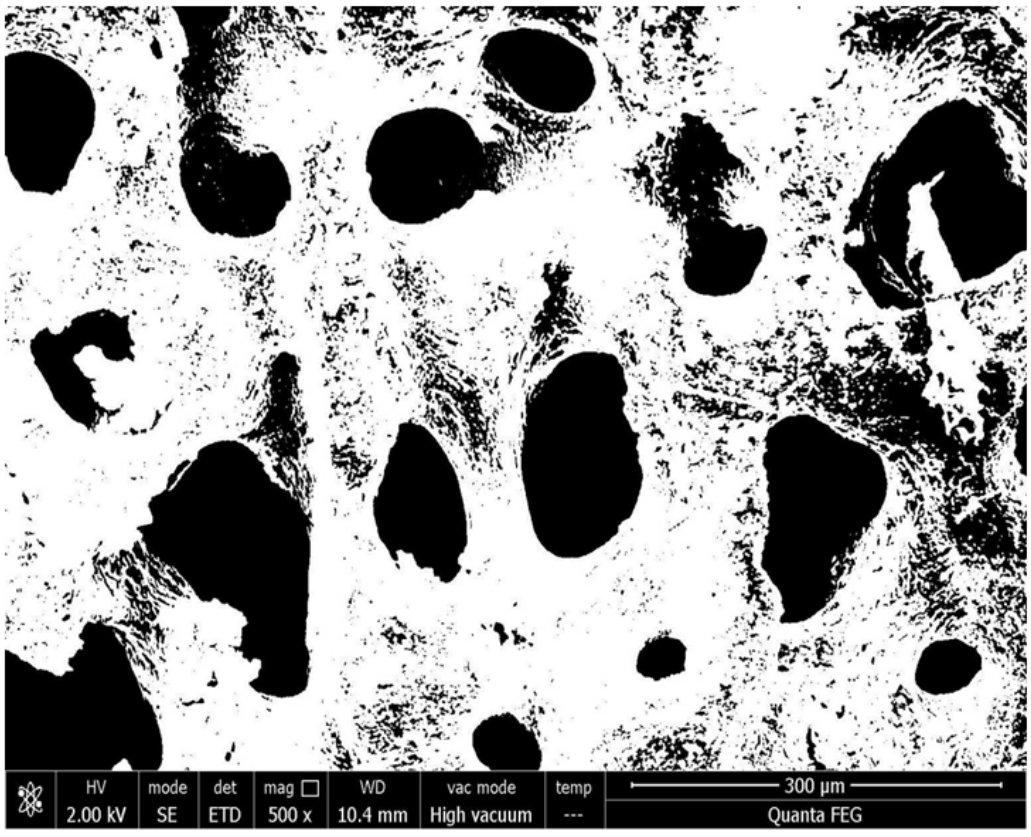

A) Pore marker of porcine compact skull bone (500×)

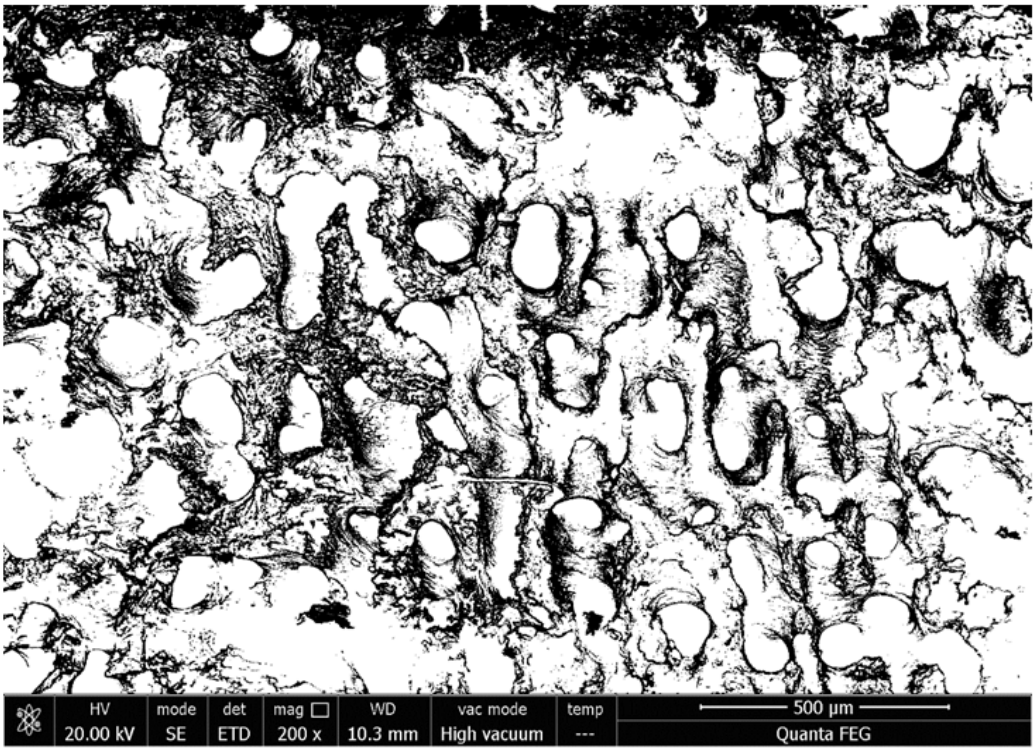

B) Pore marker of porcine compact skull bone (200×)

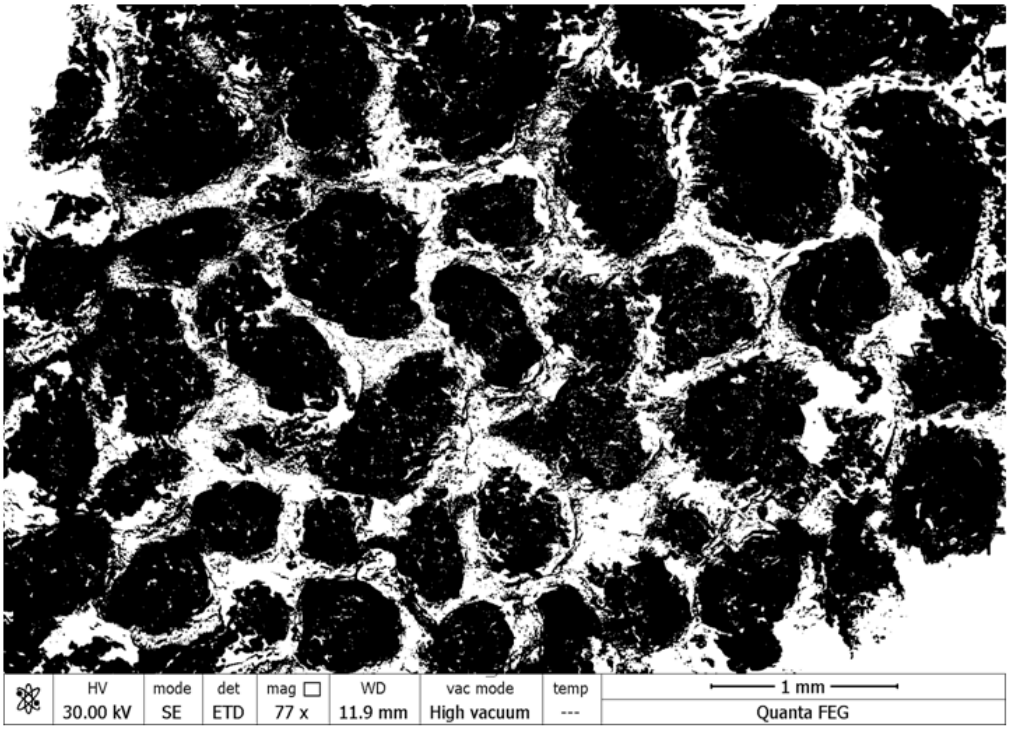

C) Pore marker of porcine cancellous skull bone (77×)

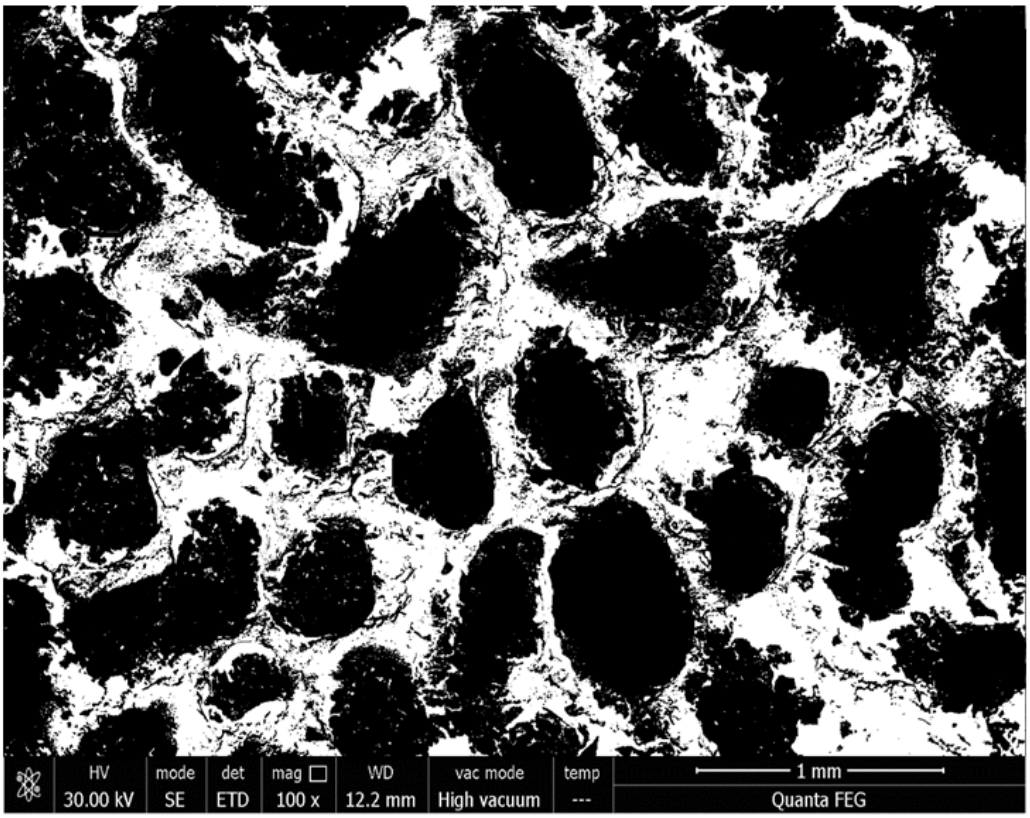

D) Pore marker of porcine cancellous skull bone (77×)

Fig. 3. Image-pro plus processing images of porcine skull samples

A) Image-Pro Plus processing images of compact bone with 500 magnification times, B) Image-Pro Plus processing images of compact bone with 200 magnification times, C) Image-Pro Plus processing images of cancellous bone with 77 magnification times, D) Image-Pro Plus processing images of compact bone with 100 magnification times. It shows that the pore structure is uniformly distributed within the skull microstructure

Table 1. Parameters (pore area, solid area and porosities) of the Micronesia porcine skull bone specimens

Skull types	Compact bone			Cancellous bone		
Items	**Pore area (mm^2)**	**Solid area (mm^2)**	**Porosity**	**Pore area (mm^2)**	**Solid area (mm^2)**	**Porosity**
First group	0.13	0.46	27.57%	7.33	11.46	63.97%
Second group	0.86	2.87	29.84%	13.61	19.28	70.60%
Third group	0.16	0.46	35.36%	8.52	11.46	74.37%
Average value	0.38	1.26	30.92±4.00%	9.82	14.06	69.65±5.27%

From Tables 1, 2 and 3, the average areas are 1.09×10^6 μm^2, 6.25×10^5 μm^2, 2.54×10^2 μm^2 and 41.50 μm^2, the mean radii are 7.38×10^2 μm, 7.46×10^2 μm, 6.40 μm and 5.75 μm, and the average radius ratios are 16.98, 9.88, 29.40 and 52.57 for 500, 200, 100 and 77 times magnification, respectively. Because not all pores are regular round pores, there is a certain radius ratio, which is the long radius divided by the short radius.

Table 2. Pore parameters (area, average radius and radius ratio) of porcine compact skull bone under different magnification

Skull types	Compact			Bone		
Items	**Area**	**Average radius**	**Radius ratio**	**Area**	**Average radius**	**Radius ratio**
Units	**μm^2**	**μm**		**μm^2**	**μm**	
Magnification		500 times			200 times	
Sample		131			17	
Minimum value	1.83×103	49.52	1.34	4.91×102	28.70	1.51
Maximum value	1.57×107	3.97×103	1.96×102	1.70×106	1.40×103	98.52
Average value	1.09×106	7.38×102	16.98	6.25×105	7.46×102	9.88
Total	1.43×107	9.67×104	2.23×103	1.06×107	1.27×104	1.68×102

Table 3. Pore parameters (area, average radius and radius ratio) of porcine cancellous skull bone under different magnification

Skull types	Cancellous			Bone		
Items	**Area**	**Average radius**	**Radius ratio**	**Area**	**Average radius**	**Radius ratio**
Units	**μm^2**	**μm**		**μm^2**	**μm**	
Magnification		77 times			100 times	
Sample		17			25	
Minimum value	4.02	1.90	2.06	1.00×10^{-3}	3.50×10^{-2}	3.50×10^{-3}
Maximum value	1.60×10^{2}	10.99	6.56×10^{2}	2.18×10^{2}	13.56	3.46×10^{2}
Average value	41.50	5.75	52.57	2.54×10^{2}	6.40	29.399
Total	7.33×10^{2}	97.73	8.93×10^{2}	1.36×10^{3}	1.60×10^{2}	7.35×10^{2}

2.2 Finite-element Analysis

From the SEM images of the porcine skull specimens, the microstructure models of cancellous and compact bones were created using the FE software ANSYS Workbench (Version 12.1, ANSYS Inc., USA). Models were analysed with and without FSI. The microstructure model of the porcine skull bone was built in the Geometry module. The geometric structure parameters were then shared with the fluid analysis module in Fluent and the stress analysis in the Static Structural module; the FSI analysis between the solid-liquid phases was undertaken by importing the fluid calculation results into the stress analysis.

According to the literatures [50-52], the microstructure of compact and cancellous skull skeleton bone were the bone plate by the cylinder shaped pipeline and the porous sponge structure by the prism shaped trabecular bone. Two types of models were solved for both compact and cancellous bone. One focused purely on structural modelling (i.e. without FSI) and the other included the effects of the fluid flow on the bone (i.e. with FSI). The boundary and initial conditions of the skull microstructure model for the fluid-structure coupling cases were as follows:

1) To simulate the changing ICP, ICPs of 2.0 kPa, 2.5 kPa, 3.0 kPa and 3.5 kPa were applied within a time of 1 s inside the models of the cancellous and compact bone (shown in Figs. 4 and 5);
2) Fixed constraints were applied at the outlet surface of the porcine skull microstructure model with the ICP stressed from the inlet surface along the direction of the *Y*-axis for cancellous bone and *X*-axis for compact bone (axes are visible in Figs. 4 and 5). At the same time, the fluid flows into the skull bone microstructural model.
3) The tissue fluid in the skull bone is laminar flow within the microstructure, and the flow parameters are as shown in Table 5.
4) The model without FSI was solved as above, but stress was applied directly at the walls of the bone rather than through the fluid.

2.2.1 Microstructure compact skull bone

Two types of models were solved for compact bone. One focused purely on structural modelling of solid skeleton bone and the other included the effects of the fluid flow of interstitial fluid in the microstructure compact skull bone.

2.2.1.1 Microstructure model of compact bone

The basic structure of compact skull bone composes mainly of the bone plate, Haversian canal and bone matrix, in which the former two constitute the Haversian system, the main parts of compact bone and bone unit. The nutrients flow within the blood vessels of the Haversian canals and are piped to supply the bone tissue and cells through the porous system composed of Haversian and Volkmann's canals. The parameters of Haversian system of skull parietal bone were shown in Table 1.

Haversian and Volkmann's canals together constitute the major microtubule system in the compact bone [7,56,57]. With the increased intracranial pressure (ICP), the tissue liquid in the Haversian canal will begin to spread and penetrate into the Volkmann's canal and other porosity, which affects the porous system of Haversian and Volkmann's canals. Within the porous system of Haversian and Volkmann's canals, the diameter and thickness of Haversian canal is 25 μm, and 3 μm, and the diameter of Volkmann's canal is 15 μm [58]. Assuming the bone interstitial fluid through the microstructure model of compact bone along the direction of *X*--axis, Inlet is named as fluid flowing into the surface and Outlet is named as fluid flowing out the surface. The parameters pass through the fluid-solid contact surface in the flow field. *F-FSI* and *S-FSI* are named as the fluid-solid contact surface separately in the interstitial fluid and solid compact parts. From the Scanning Electron Microscopy (SEM) (Electron Scanning Microscope, S-3400N, Hitachi High Technologies America, Inc.; Energy Dispersive Spectroscopy, INCA Energy 350, Oxford Instruments, UK; Media Cybernetics, Silver Spring, Maryland 20910, USA) images of the porcine skull specimens, the microstructure model of compact bone was modelled as a cylinder of length 1000 μm and diameter 100 μm, with the strut thickness of 40 μm, giving a porosity of 70% with the FE software ANSYS Workbench (Version 12.1, ANSYS Inc. USA) (Fig. 4).

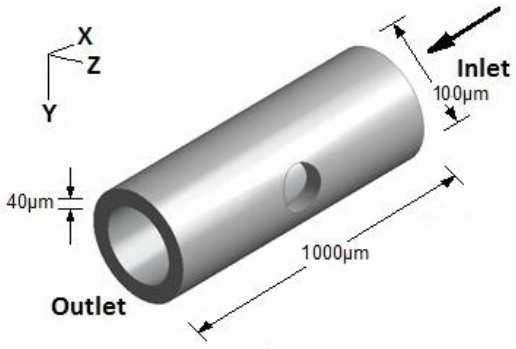

Fig. 4. Porous model of compact bone

Importing the microstructure model of compact bone into the ANSYS Fluent software (ANSYS Inc., USA) and restrained the solid compact skeleton, the fluid domain is meshed with the method of size control and grid expansion. The mesh had 109,213 nodes and the unit numbers are 130,000 by setting the mesh size of 0.001 mm (Fig. 5).

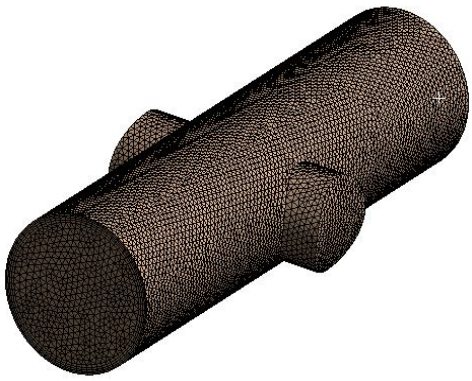

Fig. 5. Meshes of fluid domain in the microstructure compact skull bone. 109,213 nodes, 130,000 unit numbers

Table 4. Parameters (density, Poisson's ratio and elastic modulus) of porcine skull skeleton

Items	Density (kg/m^3)	Poisson's ratio	Elastic modulus (×10^9 N/m^2)
Trabecular bone [53]	1650	0.3	8
Lamella [54]	2250	0.10	38

Table 5. Flow parameters (density, viscous coefficient, inlet velocity and inner pressure) of tissue fluid in the skull bone [55]

Items	Density (kg/m^3)	Viscous coefficient (N·s^{3}m^{-2})	Inlet velocity (m/s)	Inner pressure (Pa)
Bone interstitial fluid	1050	0.4	0.02	2666

Table 6. Haversian system parameters of skull parietal bone [6]

Items	Skull bone (parietal and frontal skull)
Diameter of Haversian system (μm)	10~70
Diameter of Haversian canal (μm)	5~40
Thickness of Haversian bone plate (μm)	3
Haversian plate layer (layer)	2~6

2.2.2 Microstructure cancellous skull bone

Two types of models were solved for the microstructure of cancellous bone. One focused purely on structural modelling of solid skeleton bone and the other included the effects of the fluid flow of interstitial fluid in the microstructure skull bone. This application of linear elasticity theory and biphasic characterization requires that the pore space be characterized without mechanically influencing the solid component. In addition, the microstructural solid properties must be quantified without altering the pore space boundary.

2.2.2.1 Microstructural model of cancellous bone and ISF

According to the Wolff's law of trabecular architecture at remodeling equilibrium [59] and based on the Scanning Electron Microscopy (SEM) images of the porcine skull specimens, the microstructure of cancellous bone was chosen as the model of rod-rod structure and simulated as an open prism model which has sides of length 1000 μm, with strut thickness of 100 μm, giving a relative density of 1040 kg/m^3 and a porosity of 70%. Thus the microstructure model of cancellous bone is set up as Fig. 6. The material parameters used for the trabecular bone and lamella of the porcine skull bone are shown in Table 4.

Assuming the bone interstitial fluid through the microstructure model of cancellous bone along the direction of *Y*--axis, inlet is named as fluid flowing into the surface and outlet is named as fluid flowing out the surface. The parameters pass through the fluid-solid contact surface in the flow field. *F-FSI* and *S-FSI* are named as the fluid-solid contact surface separately in the fluid and solid parts.

Before meshing the solid skeleton of cancellous bone, the fluid domain was restrained firstly. After the material properties were assigned, the cancellous bone was meshed with the Dex Dominant Method (Fig. 7). The mesh had 68,256 nodes, and the unit numbers are 130,000 by setting the mesh size to 0.002 mm.

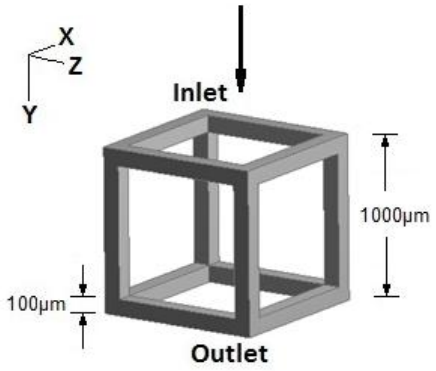

Fig. 6. Rod-rod microstructure model of cancellous bone

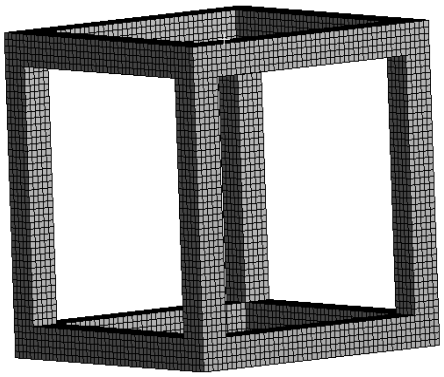

Fig. 7. Meshes of the cancellous bone model. 68,256 nodes, and 130,000 unit numbers

2.2.2.2 Fluid-structure model in the cancellous microstructure bone

The tissue fluid in the skull bone is laminar flow within the microstructure, and the flow parameters are as shown in Table 5.

In the ANSYS Workbench 12.1, the geometric model of solid domain is separated from that of fluid domain. While imported into the ANSYS Fluent software (ANSYS Inc., USA), the model is composed of solid skeleton and fluid. So the solid skeleton model needs to be compressed for meshing the remaining fluid model. For the regular geometry structure of the fluid domain in

the cancellous bone, the structure grid is suitable to mesh the fluid domain which is a regular geometry structure. The unit number of fluid grid in the cancellous microstructure bone keeps the same value at each point, so the result is more accurate to calculate the stress concentration of the boundary and surface in the fluid domain. Because the structure grids only apply to a smaller range and cannot be used for meshing of complex graphics, the regular prism structure is adopted to mesh the microstructure model of cancellous bone for getting more accurate calculation results and reducing the computation time. The Dex Dominant Method is used to mesh the fluid domain. The mesh had 38,712 nodes, and unit numbers are 35,451 by setting the grid size to 0.03 mm, shown in Fig. 8.

Fig. 8. Mesh grid of the fluid domain in the cancellous microstructure bone. 38,712 nodes, and 35,451 unit numbers

3. RESULTS

3.1 Finite-element Analysis of Compact and Cancellous Skull Bone

The results in the fluid domain were imported into the Static Structural Module in the ANSYS Workbench software (Version 12.1, ANSYS Inc. USA) to analyse the deformation of solid compact skeleton as the ICP changes. After the material parameters of compact bone were assigned to the solid skeleton, the fixed constraint was applied on the outlet surface of the microstructure compact bone, with the ICP stressed along the *X*-axis direction of 2.0 kPa, 2.5 kPa, 3.0 kPa and 3.5 kPa respectively within a time of 1 s. The fluid pressure vector was shown as Fig. 9 imported into the solid skeleton structure. And the boundary conditions of microstructure model of compact bone were shown as Fig. 10. Then the deformation nephograms of compact bone model were shown as Fig. 6 with the different ICP.

From Fig. 9, after importing the calculation results of fluid domain into the solid skeleton, the maximum pressure distributed at the junction of Harversian and Volkmann's canals and was about 5.03 Pa. The minimum pressure at the inlet was about 0.17 Pa.

From Fig. 11, the deformation of compact bone gradually increased with the raising ICP. The maximum strain was 11.9×10^{-6} at the outlet, and the minimum strain was almost no deformation at the inlet. Thus the stain distributions were uneven as the pressure stressed among the wall of microstructure compact bone. Under different pressures, the structure and material properties were the main influence factors on the compact bone deformation.

Furthermore, the fluid domain results of microstructure cancellous bone were inputted into the Static Structural Module in the ANSYS Workbench software to analyse the deformation of solid skeleton with the ICP changes. After the material parameters were assigned to the solid skeleton of cancellous bone, the fixed constraint was applied at the outlet surface of the microstructure cancellous bone, with the ICP stressed along the direction of the *Y*-axis of 2.0 kPa, 2.5 kPa, 3.0 kPa and 3.5 kPa within a time of 1 s. The fluid pressure vector was shown as Fig. 12 imported into the solid skeleton structure. And then the deformation nephograms of microstructure model of cancellous bone were in Figs. 13 and 14.

From the strains of microstructure model for cancellous bone, the deformation of skeleton skull bone was gradually increased with the raised ICP. At the same time, the strains of solid skeleton bone changed for the influence of tissue liquid flows, and the maximum strain of 2.12×10^{-4} located on the skeleton beam but the minimum strain, almost no deformation, was the skeleton bottom.

From the stress of microstructure cancellous bone, with the raised ICP, the stress on the solid skeleton bone gradually increased, and the maximum stress of 232 kPa lied in the vertical prism, but the minimum stress of 69.97×10^{-2} kPa was the beam at bottom of the skeleton bone.

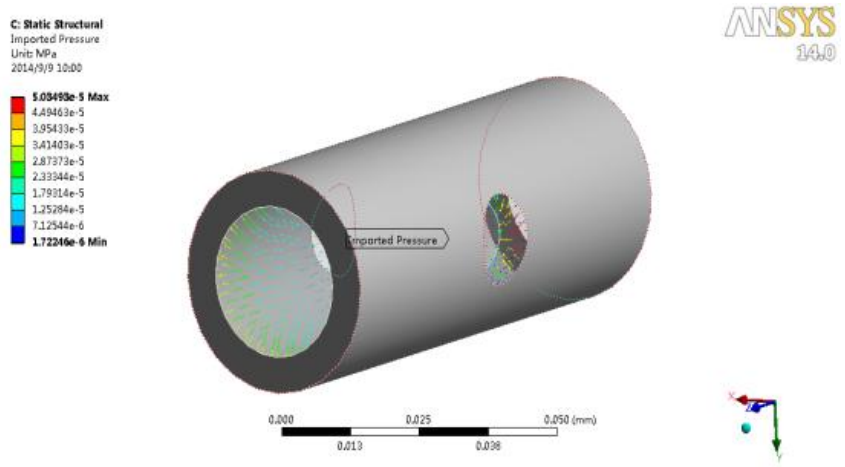

Fig. 9. Pressure in fluid domain importing the solid skeleton

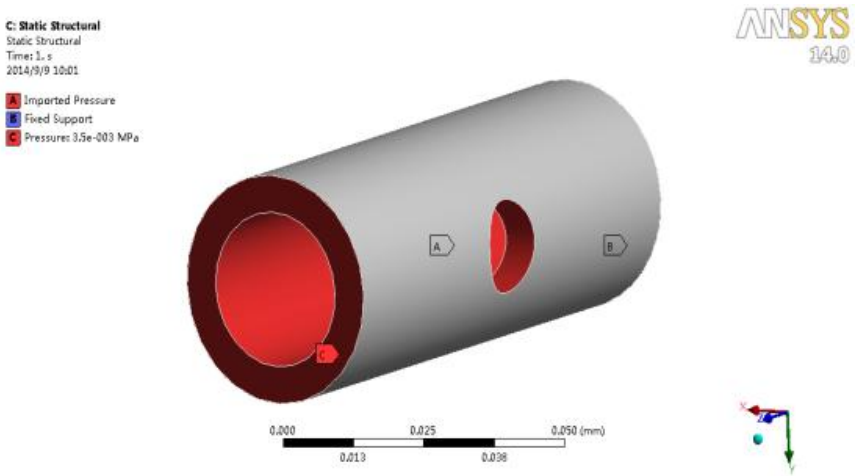

Fig. 10. Boundary conditions of Compact bone model

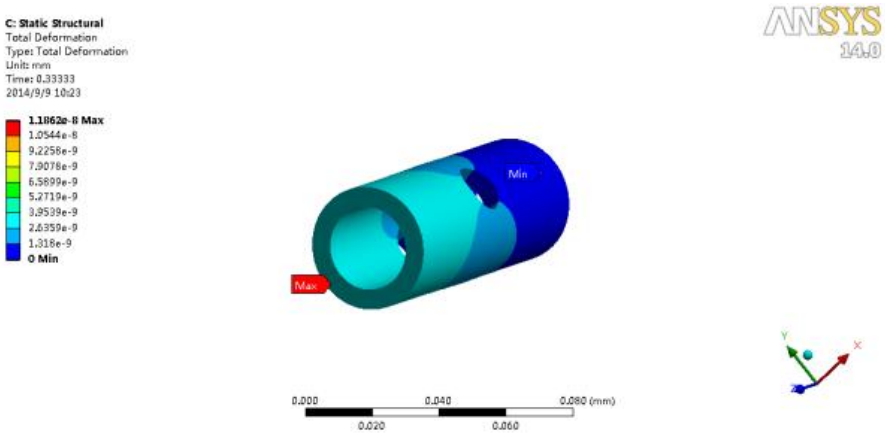

Strain nephogram of compact bone under 2.0kPa

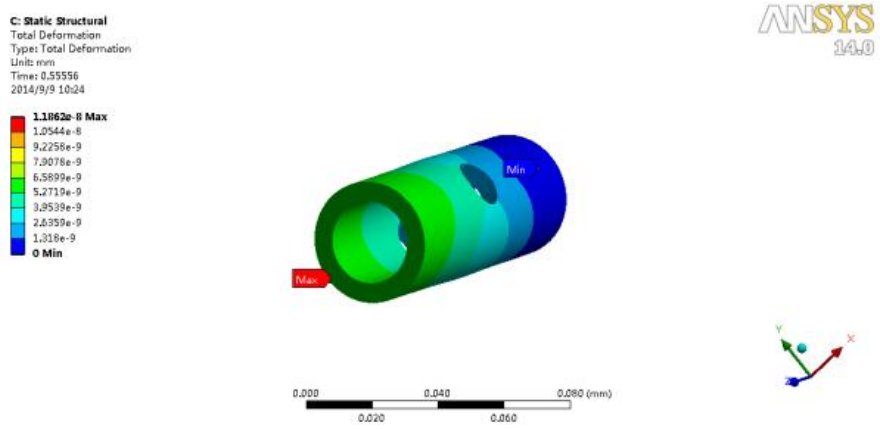

Strain nephogram of compact bone under 2.5kPa

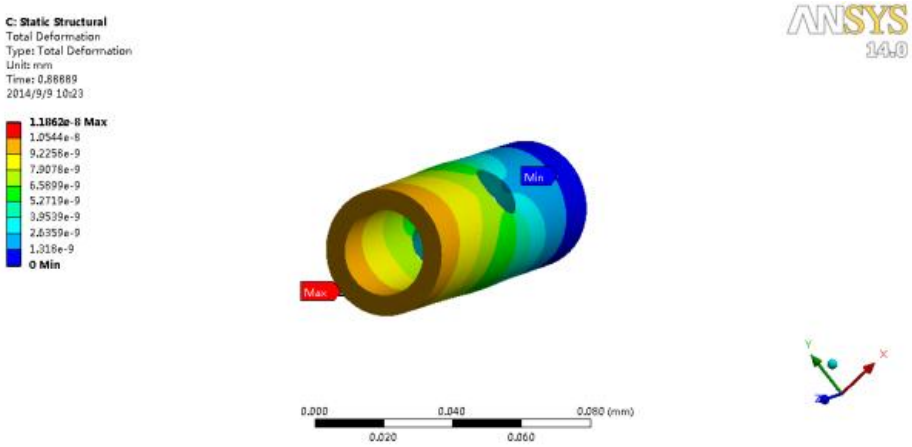

Strain nephogram of compact bone under 3.0kPa

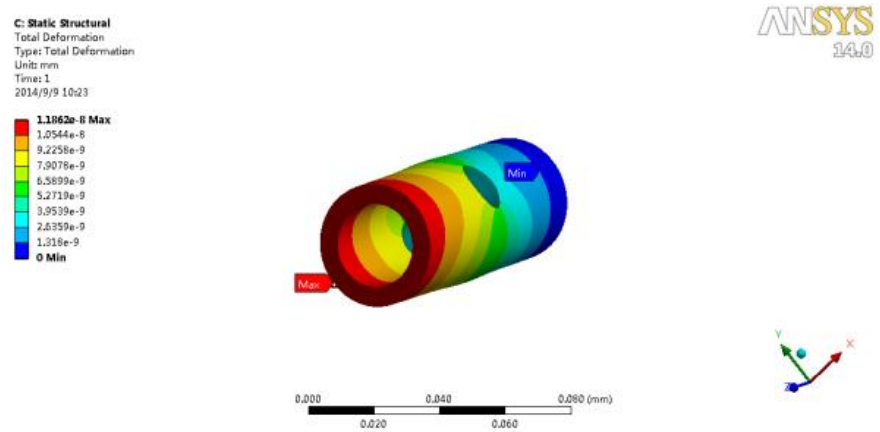

Strain nephogram of compact bone under 3.5kPa

Fig. 11. Strain nephograms of compact bone model

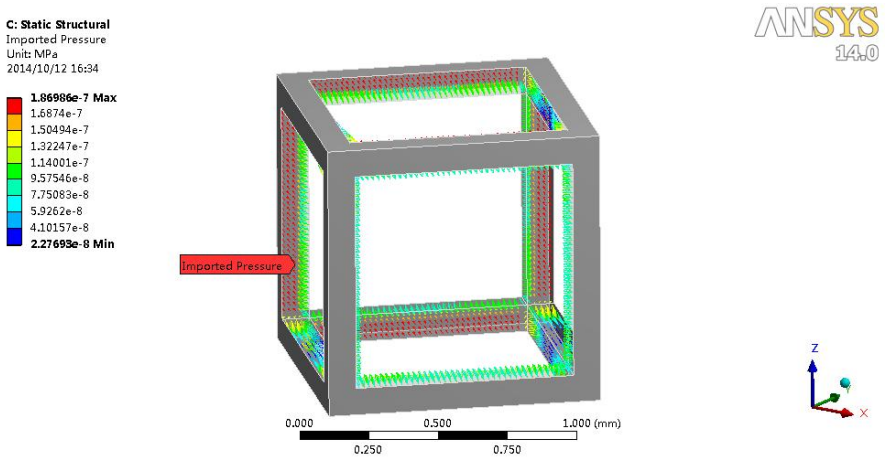

Fig. 12. Pressure nephogram of fluid importing the solid skeleton

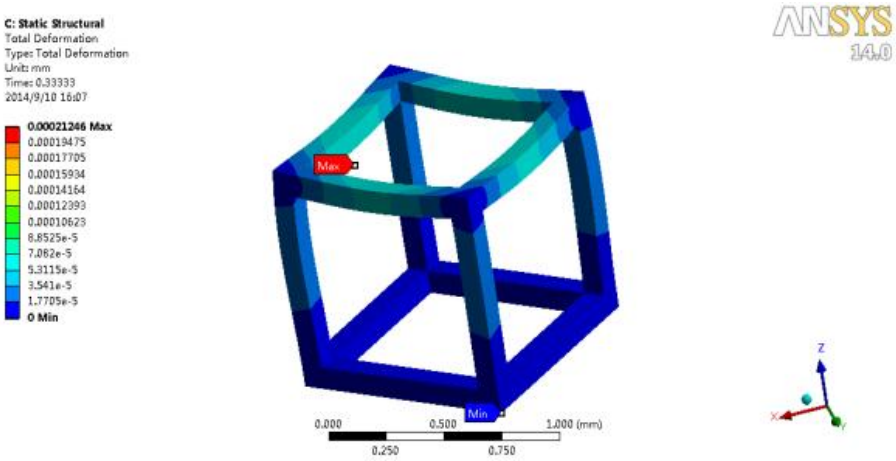

Strain nephogram of cancellous bone under 2.0kPa

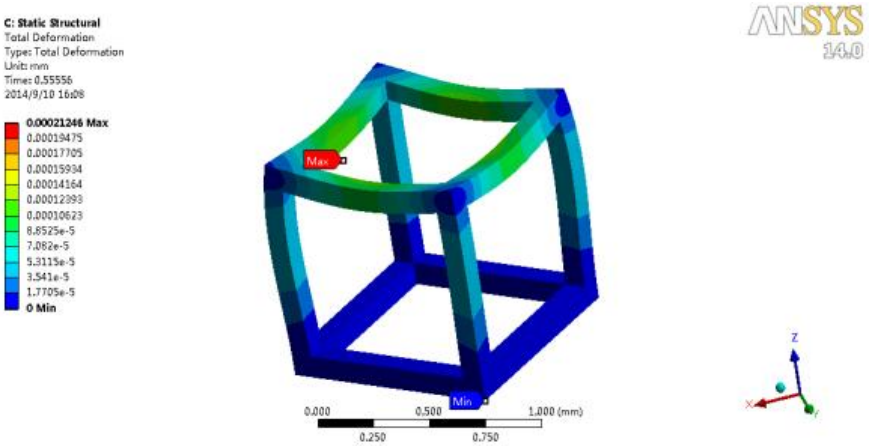

Strain nephogram of cancellous bone under 2.5kPa

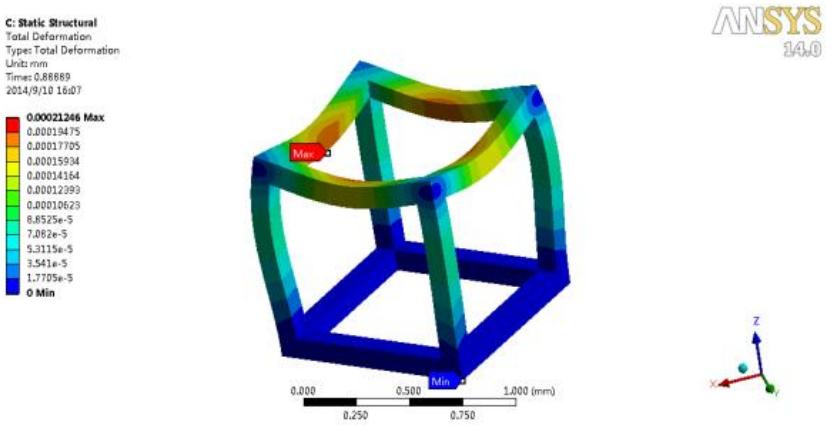

Strain nephogram of cancellous bone under 3.0kPa

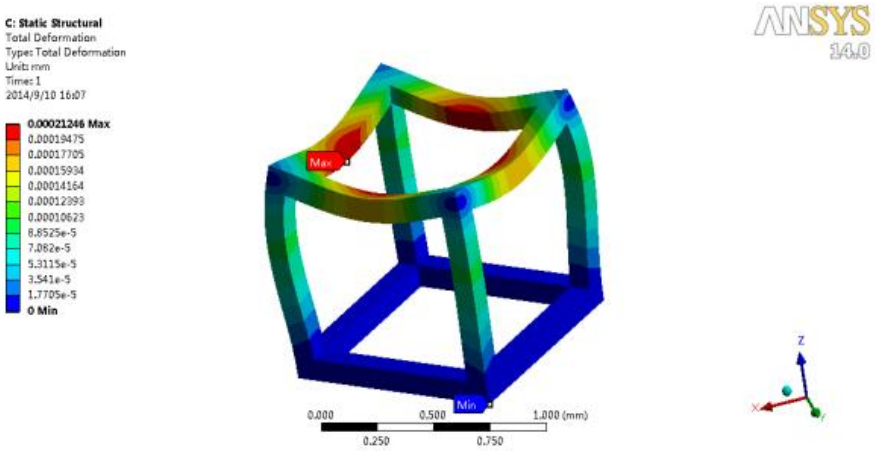

Strain nephogram of cancellous bone under 3.5kPa

Fig. 13. Strain nephograms of microstructure model for cancellous bone

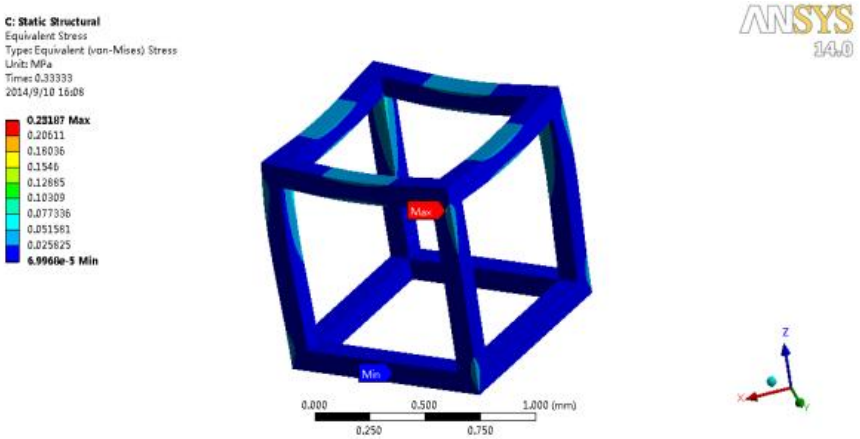

Stress nephogram of cancellous bone under 2.0kPa

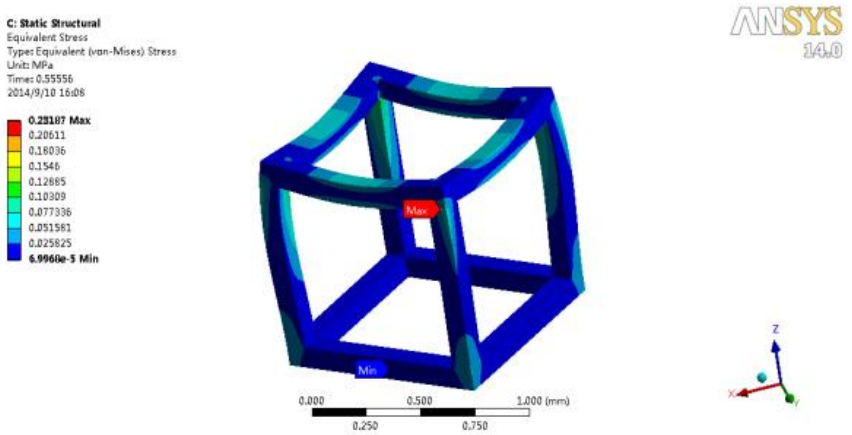

Stress nephogram of cancellous bone under 2.5kPa

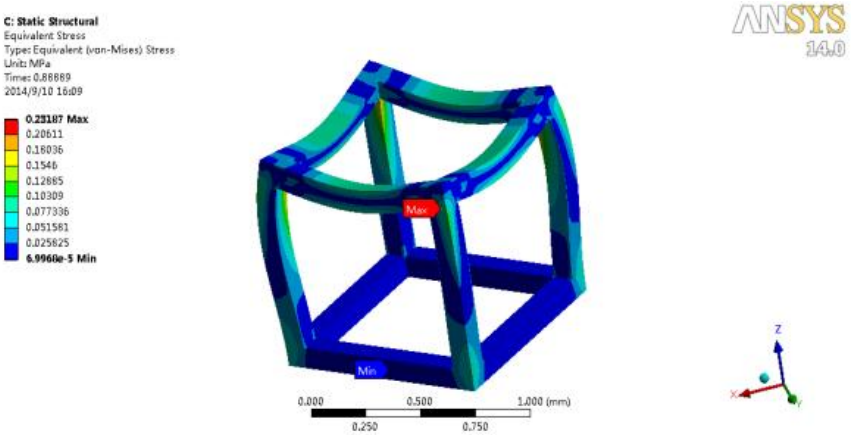

Stress nephogram of cancellous bone under 3.0kPa

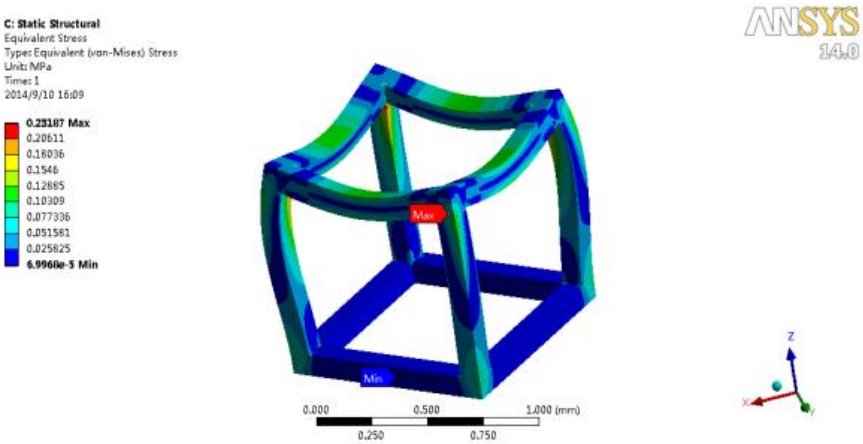

Stress nephogram of cancellous bone under 3.5kPa

Fig. 14. Stress nephograms of microstructure model for cancellous bone

The results show that with the strain and stress in the skull microstructure models increased with the rising ICP. For the microstructure of cancellous bone, the maximum deformation occurs in the middle of the bone beam and the minimum deformation occurs at the bottom of the model with the increasing ICP. Also with the interstitial fluid in the skull bone flows, the static pressure gradually increases and dynamic pressure decreases; that is, the total pressure of the interstitial fluid gradually decreases as the flow rate of interstitial fluid gradually decreases. Thus the skull bone has the properties of both solid and liquid materials, and the strain and stress curves are compared in Figs. 15 - 18 both with and without the fluid-structure interaction.

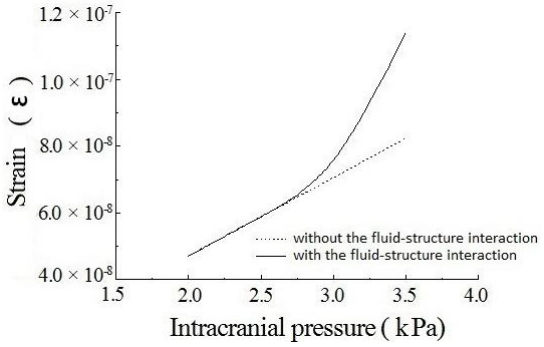

Fig. 15. Strain curves of cancellous bone with and without FSI with the ICP changes

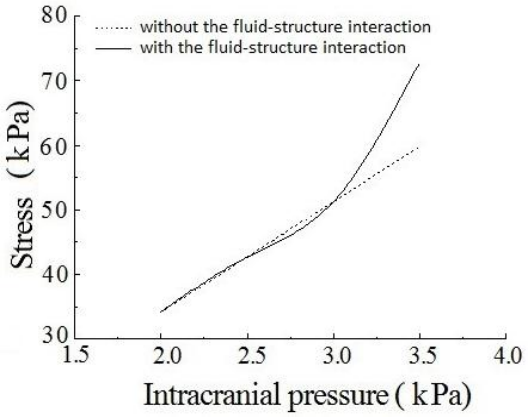

Fig. 16. Stress curves of cancellous bone with and without FSI with the ICP changes

3.2 Stress and Strain Difference of Skull Bone between with and without FSI

Comparing the strain and stress curves with and without FSI of fresh porcine skull bone microstructure shows that the deformations of the solid skeleton for cancellous and compact bone increased with ICP.

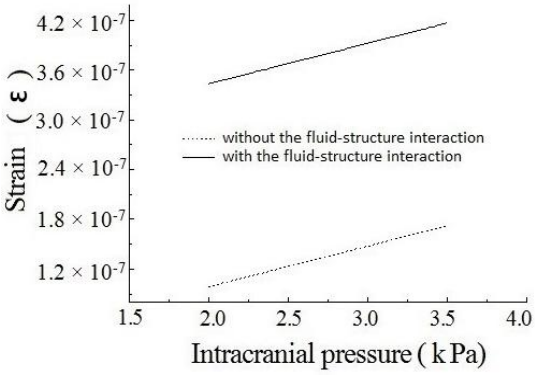

Fig. 17. Strain curves of compact bone with and without FSI with the ICP changes

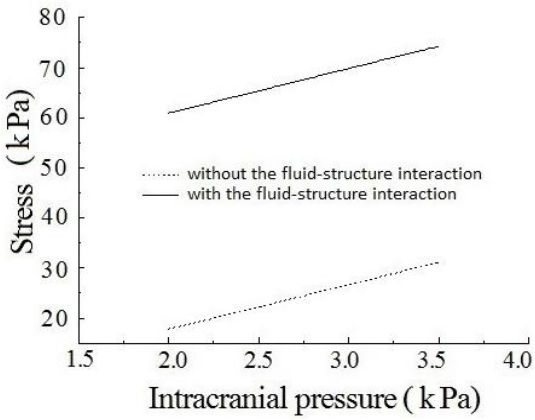

Fig. 18. Stress curves of compact bone with and without FSI with the ICP changes

The deformation rate of cancellous bone rises gradually but that of compact bone was linear. For strain, there was no difference between including and excluding FSI up to a pressure of around 2.75 kPa, and then the strain difference between the two gradually increased. Above 2.75 kPa, the strains with FSI were greater than without FSI. When the ICP reached 3.5 kPa, the maximum difference in strain between of them was 31.7 × 10^{-6}, and the strain of cancellous bone with FSI was 38.5% lower than that without FSI. Meanwhile, the stresses were the same with and without FSI of the microstructure of fresh porcine skull bone when ICP was between 2.0 kPa to 2.55 kPa. The stress difference with FSI was a little smaller than that without FSI from 2.55 kPa to 3.05 kPa, and then the stress with FSI was quickly increased above 3.05 kPa. The stress with FSI gradually increased with rising

ICP, and the maximum stress was 21.5% larger than without FSI and can be up to 72.9 kPa.

Unlike the non-linear relationship between strain and stress for FSI simulations of cancellous bone with ICP, compact bone follows a linear trend with or without FSI. The strain difference between including and excluding FSI is almost constant at 0.25×10^{-6}, and the stress difference is about 42 kPa for ICP ranging from 2.0 kPa to 3.5 kPa.

4. DISCUSSION

This study was to investigate the influence of interstitial fluid on the microstructural skeleton of compact and cancellous skull bone with the finite-element simulation as ICP changes. SEM was used to determine the microstructure of the porcine skull bone. The results were used to create a microscopic model of skull bone subjected to a FSI analysis. Then the stresses and strains of a micro structural compact and cancellous skull bone could be predicted within a one-way fluid flow regime as ICP changes. By remodelling compact and cancellous bone at the microscopic scale with finite-element method, it for the first time showed that the tissue fluid had a large influence on the microstructure of compact and cancellous skull bone when characterizing the deformation of cranial cavity and the pressure loading and bone-fluid flow can initiate and control bone morphology at the tissue level. It has been shown that the dynamic pressure significantly influences the bone-fluid flow and its associated streaming potentials, which can be controlled quantitatively [60].

The motion of intracortical fluid flow was proposed to play an important role in regulating bone mass and morphology [61]. Microdamage [60] proved that the interstitial fluid flow and mass transport were altered due to fatigue loading within bone, and the concentration and distribution of “downstream” reduced from the damage. Otter and colleagues [62] proposed that the redundant axial loading of appendicular bones led to bone perfusion. In this study, the deformation behaviour of skull bone was based on the experimental properties and investigational values on similar compact and cancellous bone types. The key findings of this study highlighted the skeleton of cranial cavity would deform under a fluid-flow stimulus. Under this condition of ICP and FSI, the strain of the microstructure bone was relatively low and most of strains were concentrated on the cancellous bone. These results also had implications for other body types, such as spine and thigh bones, whose movement mechanisms were affected by the mechanical stimuli with interstitial-fluid flow.

Furthermore, the deformation of bone tissue was enhanced with the increase of interstitial fluid under the same pressure, which would absorb more impact on cerebral injury caused by intracranial hypertension. Conversely, the load-bearing of bone tissue was enhanced with the increase of solid bone skeleton under the same pressure. In addition, by correctly computing the geometric features and analysing microstructure shapes of skull cancellous and compact bone, the surface strains were quantitatively measured and analysed and the potential abnormality and illness were likely detected. Then the FSI model simulating the skull bone would help in the development of a non-invasive device for measuring the ICP as well. Potential limitations of the current study were mainly concerned with a single microstructure of skull bone as an idealized geometry and one-way laminar flow. This model did not involve in the case when tissue fluid entered into a composite structure of compact and cancellous bone. Future studies could be implemented by incorporating composite geometries by using SEM imaging and finite-element analysis.

It showed that interstitial fluid flow played a major role in bone and osteocytes can more effectively sense the interstitial fluid flow through their processes [63-66]. The biochemical and mechanical effects of canalicular fluid flow had been investigated by many researchers [67-70], but the canalicuar fluid flow remained poorly understood which depended on the experimental and imaging difficulties to obtain accurate geometrical information and reliable material properties in vivo [71]. Model parameters are of different types, including driving gradients, geometrical, physical, and material parameters. The ‘external’ information should be provided by higher-scale models or estimated by available biological data [71]. Or the uncertainties on the physical, material, and geometrical parameters appearing at the pore scale raised an issue about the results’ reliability of the model.

5. CONCLUSION

This study aimed to contribute a better understanding of the influence of interstitial fluid flow on micro structural skull bone. To this objective, the SEM images of the porcine skull

specimens and FE software were used to define the microstructure models of skull cancellous and compact bones and developed a novel FSI model to characterize the mechanical deformation in an idealized model of skull compact and cancellous bone subject to a range of one-way fluid flow. By varying the parameters of ICP and microstructure coupling tissue fluid flow independently of one another, the analysis showed that the tissue fluid had a larger effect on the cancellous skeleton bone, but the equivalent stress on compact bone microstructure would be larger with FSI. During the analysis on mechanical properties of skull bone with FSI, the skull compact and cancellous bones were not regarded as a single phase solid structure and the porous materials characteristics must be considered. Furthermore, the strain on the microstructure bone was relatively low and much of the strain was concentrated in the skull cancellous bone under this type of loading. Thus the computational modelling of fluid-structure interaction was of importance for the microstructure of cranial cavity.

COMPETING INTERESTS

Authors have declared that no competing interests exist.

REFERENCES

1. Rangel-Castillo L, Robertson CS. Management of intracranial hyper-tension. Crit, Care Clin. 2006;22: 713–732(abstr ix).
2. Kelly DF, Goodale DB, Williams J, Herr DL, Chappell ET, Rosner MJ, Jacobson J, Levy ML, Croce MA, Maniker AH, Fulda GJ, Lovett JV, Mohan O, Narayan RK. Proposal in the treatment of moderate and severe head injury: A randomized, prospective double-blinded pilot trial. *J*. Neurosur. 1999;90:1042–1052.
3. Vincent JL, Berré J. Primer on medical management of severe brain injury. Crit. Care Med. 2005;3:1392–1399.
4. Cormio M, Gopinath SP, Valadka A, Robertson CS. Cerebral hemodynamic effects of pentobarbital coma in head-injured patients. J. Neurotrauma. 1999;16: 927–936.
5. Murray CJL, Lopez AD. The global burden of disease. 1. Harvard school of public health. 13. World Health Organization. The World Health Report: 2002: Reducing risks, promoting healthy life. 2002. World Health Organization; 1996
6. Fritton SP, Kenneth JM, Rubin CT. Quantifying the strain history of bone: Spatial uniformity and self-similarity of low magnitude strains. Journal of Biomech. Anics. 2000;33:317-325.
7. Cooper RR, Milgrain JW, Robinson RA. Morphology of the osteon. An electron microscopic study. Journal of Bone and Joint Surgery. 1966;48A:1239-1271.
8. Yue XF, Wang RN, Wang L, Liu JX. Potential therapeutic actions of hypothermia: Finite-element simulation of human skull deformation with hypothermia treatment. Proceedings of the 2010 3nd International Conference on Biomedical Engineering and Informatics. 2010;1240-1247.
9. Advani SH, Owings RP. Structural modelling of human head. J. Eng. Mech. Div., Am. Soc. Civil Eng. 1975;101:257-266
10. Charalambopoulos A, Dassios G, Fotiadis DI, Kostopoulos V, Massalas CV. On the dynamic characteristics of the human skull. Int. J. Eng. Sci. 1996;34:1339-1348.
11. Charalambopoulos A, Dassios G, Fotiadis DI, Massalas CV. The dynamic characteristics of the human skull-brain system. Math. Comp. Modelling. 1998;27: 81–101.
12. Charalambopoulos A, Dassios G, Fotiadis DI, Massalas CV. The dynamic characteristics of the human head-neck system. Int. J. Eng. Sci. 1997;35:753-768.
13. Charalambopoulos A, Fotiadis DI, Massalas CV. The effect of geometry on the dynamic characteristics of the human skull. Int. J. Eng. Sci. 1998;36(9):1047-1060.
14. Charalambopoulos A, Fotiadis DI, Massalas CY. Frequency spectrum of the bispherical hollow system: the case of the nonuniform thickness human skull. Acta Mech. 1998;130:249 -278.
15. Charalambopoulos A, Fotiadis DI, Ktena A, Massalas CV. The effect of viscoelastic brain on the dynamic characteristics of the human skull-brain system. Acta Mechanica. 1998;130:159-173.
16. Kaster T, Sack I, Samani A. Measurement of the hyperelastic properties of ex vivo brain tissue slices. J. Biomech. 2011;44(6): 1158-1163.

17. Gefen A, Margulies SS. Are in vivo and in situ brain tissues mechanically similar? J Biomech. 2004;37:1339-1352.
18. Hrapko M, et al. Characterisation of the mechanical behaviour of brain tissue in compression and shear. Biorheology. 2008;45(6):663-676.
19. Prange MT, Margulies SS. Regional, directional, and age dependent properties of the brain undergoing large deformation. J. Biomech..Eng.- Trans. ASME. 2002; 124:244–252
20. Miller K, Chinzei K. Constitutive modelling of brain tissue: experiment and theory. J. Biomech. 1997;30:1115–1121.
21. Miller K, Chinzei K. Mechanical properties of brain tissues in tension. J. Biomech. 2002;35:483–490.
22. Miller K, Taylor W, Wittek A. Mathematical models of brain deformation behaviour for computed–integrated neurosurgery, In: Research Report of Intelligent Systems for Medicine Laboratory, University of Western Australia, ISML/01/06; 2006.
23. Meaney DF. Relationship between structural modelling and hyperelastic material behavior: Application to CNS white matter. Biomech. Model. Mechanobiol. 2003;1:279–293
24. Brands DWA, Bovendeerd PHM, Wisman JSHM. On the potential importance of non-linear viscoelastic material modelling for numerical prediction of brain tissue response: test and application. Stapp Car Crash J. 2002;46:103–121.
25. Brands DWA, Peters GWM, Bovendeerd PHM. Design and numerical implementation of a 3D non-linear viscoelastic constitutive model for brain tissue during impact. J. Biomech. 2004;37: 127–134.
26. Velardi F, Fraternali F, Angelillo M. Anisotropic constitutive equations and experimental tensile behaviour of brain tissue. Biomech. Model. Mechanobiol. 2006;5:53–61.
27. Heller HC, Orians GH, Purves WK, Sadava D. Life: The science of biology, 7th Edition. Sunderland, MA: Sinauer Associates, Inc. & W. H. Freeman and Company; 2003.
28. Available:http://academic.pgcc.edu/~mhubley/a&p/205/notes/notes7.pdf
29. Juraj Artner. Atlas of Human Skeletal Anatomy. Ebook. Available:www.jurajartner.com
30. Brain and spinal cord tumors in adults. American Cancer Society.
31. Tubbs RS, Bosmia NA, Cohen-Gadol AA. The human calvaria: A review of embryology, anatomy, pathology, and molecular development. Child's Nervous System. 2011;28(1):23–31.
32. Bari ML, Patricia AR, Scott R, Ralph TH. McMinn's color atlas of head and neck antomy. Fifth Edition, Elsevier Health Sciences; 2016.
33. Aydin T. Human body dynamics: Classical mechanics and human movement; 1999. ISBN 0-387-98801-7, Springer.com
34. Juraj A. Atlas of human skeletal anatomy; 2002. eBook by *Juraj Artner.com*
35. Gray's Anatomy. 38th Edition. Churchill Livingstone, New York; 1995.
36. Piekarski K, Munro M. Transport mechanism operating between blood supply and osteocytes in long bones. Nature. 1977;269:80–82.
37. Wang L, Cowin SC, Weinbaum S, Fritton SP. Modeling tracer transport in an osteon under cyclic loading ann. Biomedical Engineering. 2000;28:1200–1209.
38. Weinbaum S, Cowin SC, Zeng Y. A model for the fluidshear stress excitation of membrane ion channels in osteocytic processes due to bone strain. In: Vander by, R. (Ed.), Advances in Bioengineering. American Society of Mechanical Engineers, NewYork. 1991;317–320.
39. Cowin SC, Weinbaum S, Zeng Yu. A case for bone canaliculias the anatomical site of strain-generated potentials. Journal of Biomechanics. 1995;28:1281–1296.
40. Burger EH, Klein Nulend J, Cowin SC. Mechanotransduction in bone. In: Zaidi, M. (Ed.), JAI Press, London. Advances in Organ Biology 5a. 1998;107–118.
41. Woster PS, LeBlanc KL. Management of elevated intracranial pressure. Clin Pharmacol. 1990;9:762.
42. Jackson SA, Piper I, Dunn L, Leffler C, Daley M. Assessment of the variation of cerebrovasculao reactive in head injured patients. Acta Neurochur (Suppl). 2000;76: 445-449.
43. Citerio G, Andrews PJ. Intracranial pressure. Part two: Clinical applications and technology. Intensive Care Med. 2004; 30:1882-1885.
44. Miller JD, Becker DP, Ward JD, Sullivan HG, Adams WE, Rosner MJ. Significance of intracranial hypertension in severe head injury. Journal of Neurosurgery. 1977;47: 503-516.

45. Yue XF, Wang L, Wang RN. Tissue modeling and analyzing with finite element method: A review for cranium brain imaging. International Journal of Biomedical Imaging. 2013;12:1-12.
46. Boyde A. Scanning electron mocroscopy of bone. Methods Mol Biol. 2012;816:365-400
47. Rahul S, Amar G, Anand P. Finite element analysis of human clavicle bone: A methodology review. American Journal of Mechanical Engineering and Automation. 2014;1(5):54-59.
48. Mythily S, Daniel S, Scott J. Effect of fixatives and tissue processing on the content and integrity of nuclieic acids. Am J Pathol. 2002;161(6):1961-1971.
49. Florian H. How to prepare your specimen for immunofluorescence microscopy. Available:www.leica-microsystems.com
50. Beaupre GS, Hayes WC. Finite element analysis of a three-dimension open-celled model for trabecular bone. Transaction of ASME. J. Biomech. Eng. 1985;107:249-256.
51. Chiara VB, Francesco B, Enrica V. High strength bioactive glass-ceramic scaffolds for bone regeneration. Journal of Materials Science: Materials in Medicine. 2009; 20(2):643-653.
52. Boonlom T, Nattapon C, Kriskrai S, George AT, Chen QZ. Bone tissue engineering scaffolding: Computer-aided scaffolding techniques. Prog Biomater. 2014; 3:61-102.
53. Jackson SA, Piper I, Dunn L, Leffler C, Daley M. Assessment of the variation of cerebrovasculao reactive in head injured patients. Acta Neurochur (Suppl). 2000; 76:445-449.
54. Citerio G, Andrews PJ. Intracranial pressure. Part two: Clinical applications and technology. Intensive Care Med. 2004; 30:1882-1885.
55. Voo L, Kumaresan S, Pintar FA, Yoganandan N, Scnces Jr. A. Finite-element models of the human head. Med. & Biol. Eng. & Comput. 1996;34:375-381.
56. Boyde A. Scanning electron microscope studies of bone. In: Bourne, G. H. (Ed), The Biochemistry and Physiology of Bone. Academic Press, New York. 1972;290.
57. Jiang JZ, Jia C, Guo YS. Numerical simulation of flow field for tissue engineering scaffold microtubules. Chemical Industry and Engineering Progress. 2014;33(7):1850-1855.
58. Atkinson PJ, Hallsworth AS. The spatial structure of bone. In: Harrison J. Navaratlnan, V. (eds), Progress in Anatomy. Cambridge University Press, Cambridge. 1982;2:179-199.
59. Reich KM, Frangos JA. Protein kinase C mediates flow-induced prostaglandin E_2 production in osteoblasts. Calc. Tissue Int. 1993;52:62-66.
60. Boyce TM, Fyhrie DP, Glotkowski MC, Radin EL, Schaffler MB. Damage type and strain mode associations in human compact bone bending fatigue. J. Orthop. Res. 1998;16:322-329.
61. Li P, Liu C, Hu M, Long M, Zhang D, Huo B. Fluid flow-induced calcium response in osteoclasts: Signaling pathways. Ann Biomed Eng. 2014;42: 1250-1260.
62. Otter MW, Qin YX, Rubin CT, McLeod KJ. Does bone perfusion/ reperfusion initiate bone remodeling and the stress fracture syndrome? Med. Hypotheses. 1999;53: 363.
63. Buckwalter JA, Glimcher MJ, Cooper RR, Recker R. Bone biology part I: Structure, blood supply, cells, matrix, and mineralization. J Bone Joint Surg. 1995a; 77(A8):1256-1275.
64. Buckwalter JA, Glimcher MJ, Cooper RR, Recker R. Bone biology part II: Formation, form, modelling, remodelling, and regulation of cell function. J Bone Joint Surg. 1995a;77(A8):1276-1289.
65. Han Y, Cowin SC, Schaffler MB, Weinbaum S. Mechanotransduction and strain amplification in osteocyte cell processes. P Natl Acad Sci USA. 2004; 101(47):16689-16694.
66. Adachi T, Aonuma Y, Tanaka M, Hojo M, Takano YT, Kamioka H. Calcium response in single osteocytes to locally applied mechanical stimulus: Differences in cell process and cell body. J Biomech. 2009b;42(12):1989-1995.
67. Adachi T, Aonuma Y, Ito SI, Tanaka M, Hojo M, Takano YT, Kamioka H. Osteocyte calcium signalling response to bone matrix deformation. J Biomech. 2009a;42(1):2507–2512.

68. Klein NJ, Nijweide PJ, Burger EH. Osteocyte and bone structure. Curr Osteoporos Rep. 2003;1(1):5–10.
69. Knothe TML. Whither flows the fluid in bone? An osteocyte's perspective. J Biomech. 2003;36:1409–1424.
70. Fritton SP, Weinbaum S. Fluid and solute transport in bone: Flow-induced mechanotransduction. Annu Rev Fluid Mech. 2009;41:347–374.
71. Vittorio S, Joanna K, Salah N, Thibault L. Interstitial fluid flow within bone canaliculi and electro-chemo-mechanical features of the canalicular milieu. Biomech Model Mechanobiol. 2013;12: 533-553.

Peer-review history:
The peer review history for this paper can be accessed here:
http://sciencedomain.org/review-history/19675